arXiv:1005.0056v1 [astro-ph.HE] 1 May 2010

Suzaku Observations of the Great Annihilator and the Surrounding Diffuse Emissions

Shinya Nakashima, Masayoshi Nobukawa, Takeshi Go Tsuru, Katsuji Koyama

Department of Physics, Graduate School of Science, Kyoto University, Sakyo-ku, Kyoto 606-8502

shinya@cr.scphys.kyoto-u.ac.jp

and

Hideki Uchiyama

Department of Physics, The University of Tokyo, 7-3-1 Hongo, Bunkyo-ku, Tokyo 113-0033

Abstract

We report the Suzaku observation of 1E 1740.7−2942, a black hole candidate called the "Great Annihilator" (GA). The high-quality spectrum of Suzaku provides the severest constraints on the parameters of the GA. Two clumpy structures are found around the GA in the line images of Fe I Kα at 6.4 keV and S XV Kα at 2.45 keV. One clump named M 359.23−0.04 exhibits the 6.4-keV line with an equivalent width of $\sim$ 1.2 keV, and is associated with a molecular cloud in the radio CS(J=1–0) map. Thus the 6.4-keV line from M 359.23−0.04 is likely due to X-ray fluorescence irradiated by an external X-ray source. The irradiating X-rays would be either the past flare of Sagittarius A* or the bright nearby source, the GA. The other clump named G 359.12−0.05 is associated with the radio supernova remnant candidate G 359.07−0.02. We therefore propose that G 359.12−0.05 is an X-ray counterpart of G 359.07−0.02. G 359.12−0.05 has a thin thermal plasma spectrum with a temperature of $kT \sim 0.9$ keV. The plasma parameters of G 359.12−0.05 are consistent with those of a single supernova remnant in the Galactic center region.

Key words: Galaxy: center—ISM: clouds—ISM: supernova remnants—X-rays: individual (Great Annihilator)

1. Introduction

The Galactic center (GC) region has many celestial objects such as a supermassive black hole Sagittarius A* (Sgr A*), star-forming regions, dense molecular clouds (MCs). The GC region is also full of high-energy phenomena. For example, several supernova remnants (SNRs) or candidates have been recently found (e.g., Nobukawa et al. 2008; Mori et al. 2008; Sawada et al. 2009; Tsuru et al. 2009). The most characteristic phenomenon is the diffuse 6.7-keV lines from highly ionized irons (Koyama et al. 1989; Yamauchi et al. 1990). The origin of this emission is probably due to a plasma with $kT \sim 6.5$ keV temperature (Koyama et al. 2007b), but is still a debatable issue. Another notable feature in the GC region is the clumpy 6.4-keV lines from neutral irons (e.g., Koyama et al. 1996). The origin is considered as MCs illuminated by X-rays or electrons. Some of the 6.4-keV clumps are well explained by the irradiation of the past X-ray flare from Sgr A* (e.g., Nobukawa et al. 2008; Inui et al. 2009; Nakajima et al. 2009).

1E 1740.7−2942 was discovered by the Einstein observatory (Hertz & Grindlay 1984) in the direction of the GC region, and was found to be the brightest GC source at above 20 keV (Skinner et al. 1987; Sunyaev et al. 1991). The time variation of the flux and the spectrum of 1E 1740.7−2942 are similar to those of Cygnus X-1, the archetypal black hole candidate, and

hence 1E 1740.7−2942 has been considered to be a black hole candidate (Cook et al. 1991; Skinner et al. 1991).

GRANAT detected a prominent bump on the spectrum of 1E 1740.7−2942 at 300–600 keV, which was interpreted as an electron-positron annihilation line at 511 keV (Bouchet et al. 1991; Sunyaev et al. 1991; Churazov et al. 1993a; Cordier et al. 1993). Thus 1E 1740.7−2942 is named the "Great Annihilator" (GA). However, no evidence for the annihilation line has been found so far by other satellites (Harris et al. 1994; Jung et al. 1995; Smith et al. 1996; Cheng et al. 1998; Bouchet et al. 2009).

The VLA radio observations discovered a radio counterpart of the GA and non-thermal double jet-like structures emanating from the GA (Mirabel et al. 1992), and hence the GA is a "micro quasar". Like the other Galactic jet sources, the GA would be a binary system with a stellar-mass black hole. In fact, the possible orbital period of 12.73 days was discovered by Smith et al. (2002). However, no clear companion star was found with the optical, infrared or radio observations, due mainly to the strong interstellar absorption toward the GC region (e.g., Eikenberry et al. 2001).

The X-ray spectrum of the GA below 10 keV is explained by an absorbed power-law model (Sakano et al. 1999; Gallo & Fender 2002). Cui et al. (2001) reported the extended X-ray emission which is perpendicular to the radio-jets (but see Gallo & Fender 2002). On the other hand, the INTEGRAL observations suggested that the

spectrum in the 10–100 keV band is explained by a model of either a comptonized-plasma plus a power-law or two comptonized-plasmas (Bouchet et al. 2009).

The radio observations found a giant MC near the GA (Bally & Leventhal 1991; Mirabel et al. 1991). Then the authors proposed the Bondi-Hoyle accretion mechanism (Bondi & Hoyle 1944); the GA is in the MC, and is powered by the gas accretion from the MC. However the ASCA observations found no clear evidence for dense gas around the GA (Churazov et al. 1996; Sakano et al. 1999).

In order to investigate the accretion mechanisms, whether the Bondi-Hoyle process, due to a binary companion or else, we performed the Suzaku observation on the GA, with its high-quality spectrum and low background. The other objective of the observation is to discover local structures, if any, on the GA and in the close vicinity of the GA, and investigate the physical relation to the GA. We assume the distance to the GC to be 8.5 kpc in this paper.

2. Observations and Data Reduction

Two pointing observations toward the GA were performed in September 2008 with the X-ray Imaging Spectrometer (XIS: Koyama et al. 2007a) at the focal plane of the X-Ray Telescope (XRT: Serlemitsos et al. 2007) on board the Suzaku satellite (Mitsuda et al. 2007). The observation log is given in table 1.

The XIS system consists of three sets of front-illuminated (FI) CCD cameras (XIS 0, 2 and 3) and one set of a back-illuminated (BI) CCD camera (XIS 1). The performance of the CCD cameras has been gradually degraded due to the radiation damage by cosmic-ray particles, thus the Spaced-row Charge Injection (SCI) technique was introduced to restore the energy resolution since October 2006 (Uchiyama et al. 2009). Thanks to the SCI, XIS energy resolutions (FI/BI) at 5.9 keV were 155/175 eV (FWHM) during the observations. However, XIS 2 is unusable for scientific observations because of the sudden anomaly in 2006, and we use the data from the remaining three cameras.

The XRT consists of closely nested thin-foil reflectors and has large collecting efficiency (450 cm^2 at 1.5 keV and 250 cm^2 at 7 keV per XRT). The point-spread function (PSF) of the XRT is about $2'$ in a half-power diameter. Each CCD camera has the $17'.8 \times 17'.8$ field of view. The band pass of the XIS+XRT is 0.3–12 keV.

The observations were carried out using the normal clocking mode with no window/burst option. The data were screened with the processing version 2.2.11.22[1] to exclude the events taken during passages of the South Atlantic Anomaly, the Night-earth elevation angle $< 5°$, and the Day-earth elevation angle $< 20°$. The effective exposures of the screened data are listed in table 1.
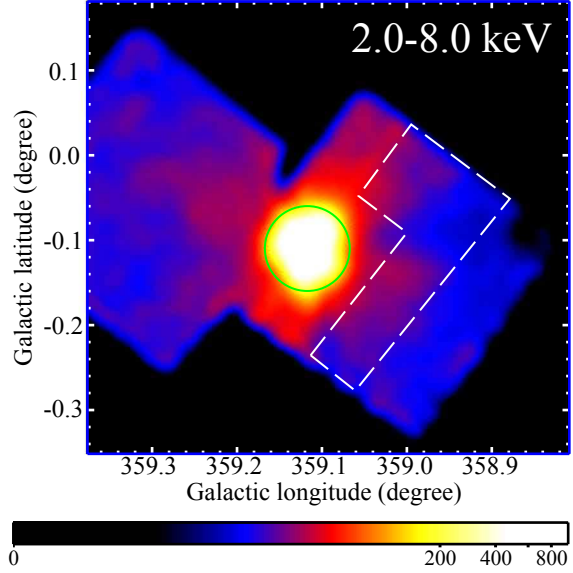
Fig. 1. The XIS image in the 2.0–8.0 keV band smoothed with a Gaussian kernel of $\sigma = 1'$. The NXB is subtracted and the vignetting effect is corrected. The green solid line indicates the source region of the GA, while the white dashed line indicates the background region of the GA. The color scale is logarithmic in units of counts bin^{-1} (the bin size is $12''.5 \times 12''.5$).

3. Analysis and Results

The analysis is made with HEASoft version 6.7[2] and XSPEC version 12.5.1[3]. The non–X-ray background (NXB) is constructed using `xisnxbgen`, and is subtracted from the data. For the model fitting of the spectrum, we generate redistribution matrix files and auxiliary response functions using `xisrmfgen` and `xissimarfgen`, respectively. We fit the FI and BI spectra simultaneously, where the FI data of XIS 0 and 3 are combined.

3.1. Wide Band X-ray Image

In order to see the overall structure, we show the 2.0–8.0 keV band image in figure 1, where all the CCDs data are merged and the calibration source regions are removed. For visibility, we sum 12×12 pixels ($12''.5 \times 12''.5$) and convolve with a Gaussian kernel of $\sigma = 1'$. In figure 1, we find a bright source at $(\alpha, \delta)_{\mathrm{J2000.0}} = (265°.9829, -29°.7462)$ of the Suzaku coordinates. Since this position coincides with the GA position of $(\alpha, \delta)_{\mathrm{J2000.0}} = (265°.9758, -29°.7501)$ (Muno et al. 2006) within the Suzaku nominal error of $19''$ (Uchiyama et al. 2008), we identify this source as the GA. We then fine-tune the Suzaku coordinates by shifting $\Delta(\alpha, \delta) = (-0°.0071, -0°.0039)$.

In figure 1, we also see local structures around the GA, partly due to the tail (spill-over) of the PSF of the XRT, but some are real X-ray structures. The major X-ray

Table 1. Observation log

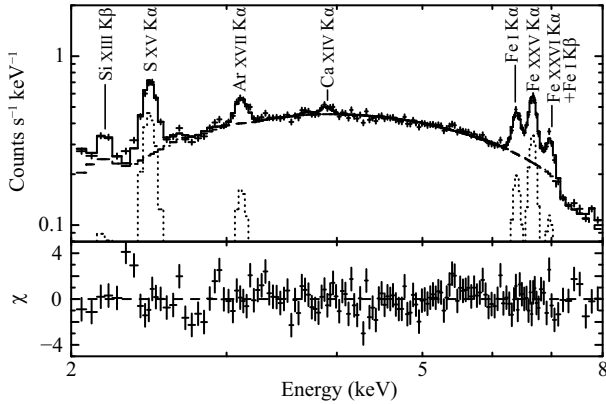| Target name	Observation ID	Pointing direction		Observation date	Exposure
		α (J2000.0)	δ (J2000.0)		(ks)
GC_LARGEPROGECT4	503010010	$17^{\rm h}44^{\rm m}10^{\rm s}$	$-29°33'20''$	2008-09-06	53.1
GC_LARGEPROGECT5	503011010	$17^{\rm h}43^{\rm m}47^{\rm s}$	$-29°49'59''$	2008-09-08	57.6

Fig. 2. The XIS FI spectrum extracted from the entire field shown in figure 1 without the 3′-radius circle centered at the GA and calibration source regions. The NXB is subtracted. The dashed line is the best-fit continuum (absorbed power-law) and the dotted lines are those of the Gaussian lines (see text).

emissions around the GA are the Galactic Center Diffuse X-rays (GCDX: Koyama et al. 1996). The GCDX is characterized by the strong lines of Fe I Kα, S XV Kα, and Fe XXV Kα at the respective energies of 6.4 keV, 2.45 keV and 6.7 keV.

In order to investigate the fluxes of the prominent lines and their spatial variations in the observed field, we make the 2.0–8.0 keV band spectrum from the entire field shown in figure 1 except the 3′-radius circle centered at the GA and the calibration source regions. The spectrum is shown in figure 2. We fit the spectrum with a phenomenological model of an absorbed power-law continuum plus Gaussian lines. We hereafter use the cross sections from Bałucinska-Church & McCammon (1992) with the solar abundance (Anders & Grevesse 1989). Then we see prominent lines at 6.4 keV, 2.45 keV and 6.7 keV above the best-fit continuum (dashed line in figure 2).

The 6.4-keV line comes from MCs and hence has clumpy spatial distribution (the 6.4-keV clumps, e.g., Koyama et al. 1996; Murakami et al. 2000; Ryu et al. 2009), while the 6.7-keV line comes from the $kT \sim 6.5$ keV plasma (the 6.5-keV plasma) and is reported to be more uniform. The 2.45-keV line is due to another hot plasma with the temperature of $kT \sim 1$ keV(the 1-keV plasma), which is not as uniform as the 6.5-keV plasma but is less clumpy than the 6.4-keV line (Ryu et al. 2009). Thus either the 6.4-keV line or the 1-keV plasma may contribute to the local structures.

3.2. Line Images

In order to depict the local structures, we use the 2.45-keV, 6.4-keV and 6.7-keV lines. To make the 2.45-keV line image, we subtract the continuum flux in the 2.7–3.0 keV (continuum-dominant band) image from the 2.35–2.55 keV (line-dominant band) image by normalizing the continuum flux ratio to that estimated from the best-fit continuum (absorbed power-law, see figure 2).

As for the 6.4-keV and 6.7-keV line images, we use the line-dominant bands of 6.3–6.5 keV and 6.6–6.8 keV, respectively, and subtract the continuum-dominant flux in the 5.0–6.0 keV band with the same method as the 2.45-keV line image. The continuum-subtracted line images are shown in figure 3, where the 3′-radius circle centered at the GA is excluded to emphasize the surrounding structures. We correct the vignetting effect and smooth with a Gaussian kernel of $\sigma = 1'$.

In the 2.45-keV line image (figure 3a), we find a diffuse structure ($16' \times 24'$) surrounding the GA, which is larger than the X-ray halo ($40''$) reported by Gallo & Fender (2002). From the center position, we name this structure G 359.12−0.05. In the 6.4-keV line image (figure 3b), we find a clump in the north (left-side of figure 3b) of the GA, and name the clump M 359.23−0.04. We note that no local structure in the 6.7-keV line image (figure 3c) is found. This supports that the 6.7-keV line (the 6.5-keV plasma) is uniform, at least near and around the GA.

3.3. Light Curve and Spectrum of the Great Annihilator

A light curve in the 2.0–8.0 keV band is made from the 3′-radius circle centered at the GA (figure 1). No significant periodicity is found in the light curve in the time range of 8–10000 sec. Also, no flux-variation larger than 10% is found in the time scale longer than 512 sec.

We therefore sum the data in all the observations and make the X-ray spectrum from the source region (the solid circle in figure 1). The background spectrum made from the dashed box in figure 1 is subtracted after correcting the difference of the effective area. For the correction of the effective area, we take into account the energy dependence of the effective area with the method given in Hyodo et al. (2008). We then fit the 2.5–12.0 keV band spectrum with an absorbed power-law model. Since a clear iron absorption edge at 7.1 keV is found, the iron abundance for the photoelectric absorption is treated as a free parameter, although the abundances of the other elements are fixed to the solar values. We find an excess bump at 3.2 keV, which may be the calibration error of the XRT Au M-II edge (Kubota et al. 2007). Thus we add a Gaussian at this energy with the fixed line-width of 0.1 keV (1 σ). Since the 6.4-keV line carries important information for the cir-
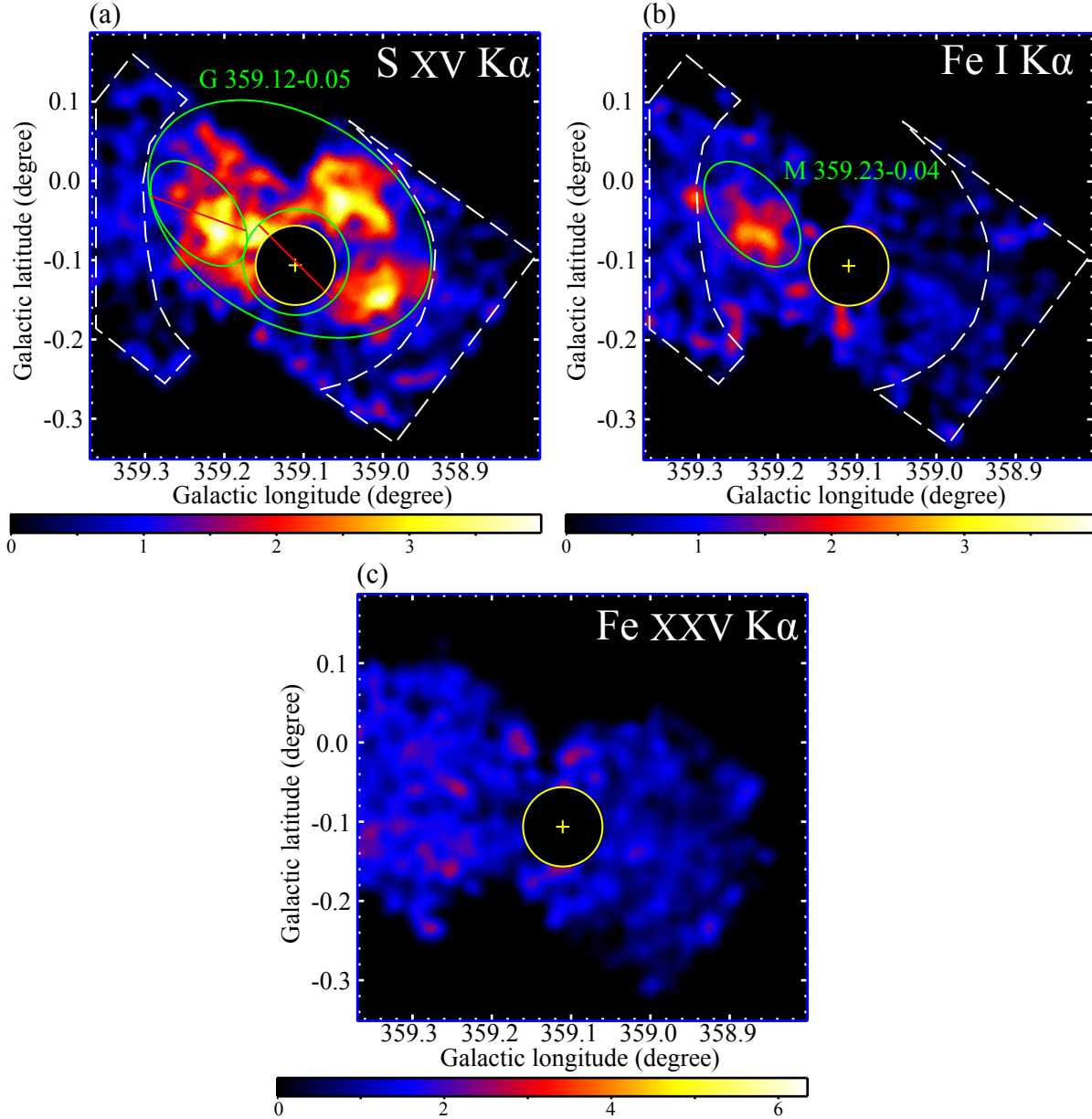
Fig. 3. The continuum-subtracted (see text) images around the GA (the yellow cross) in the S XV Kα line (a), Fe I Kα line (b), and Fe XXV Kα line (c), where the $3'$-radius regions (the yellow circle) centered at the GA are excluded. The vignetting effect is corrected, and the images are smoothed with a Gaussian kernel of $\sigma = 1'$. The green solid lines and the white dashed lines indicate the source and the background regions, respectively. The region of G 359.12−0.05 is a $16' \times 24'$ ellipse excluding the circle of $4'$-radius centered at the GA and the ellipse of the other source M 359.23−0.04 (shown in (a)). The region of M 359.23−0.04 is a $5' \times 9'$ ellipse (shown in (b)). The color scales are liner in units of 10^{-5} counts s^{-1} bin^{-1} (the bin size is $12\rlap{.}''5 \times 12\rlap{.}''5$).

cumstellar gas around the GA (e.g., Churazov et al. 1996; Sakano et al. 1999), we add a Gaussian line at 6.4 keV and fit the spectrum. Then we constrain the upper-limit of the equivalent width at 6.4 keV ($EW_{6.4\,\mathrm{keV}}$) to be < 7.8 eV at the 90% confidence level. The best-fit spectrum and the best-fit parameters are shown in figure 4 and in table 2, respectively. Note that we show only the FI spectrum in figure 4 for simplicity, although the FI and BI spectra are fitted simultaneously.

The error due to possible flux variation in the back-

ground spectrum would be small, because the background spectrum is made from the region where the 6.4-keV-line flux is smoothly distributed (see figure 3b). For a more quantitative estimate, we drive the 6.4-keV-line flux in every $3'$-radius segment in the entire region of figure 3b, excluding the areas of the GA and M 359.23−0.04. Then we find that the flux-variation of the 6.4-keV line is within $\sim 1.1 \times 10^{-3}$ counts s^{-1} (90% confidence). This value is about 1/5 of the upper limit of the 6.4-keV-line flux from the GA ($\sim 5.8 \times 10^{-3}$ counts s^{-1}). Adding this error due
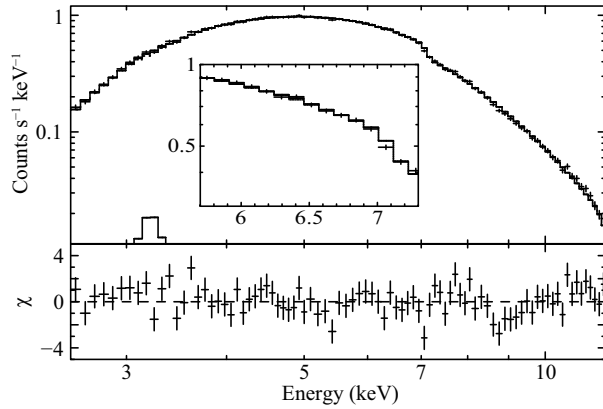
Fig. 4. The XIS FI background-subtracted spectrum of the GA in the 2.5–12 keV band with the logarithmic scales for both the horizontal and vertical axes. The enlarged spectrum in the 5.7–7.3 keV band is given in the inset, where the horizontal axis is liner and the vertical axis is logarithmic. We see no line-like structure at 6.4 keV (see text).

Table 2. Best-fit parameters of the GA

Parameter	Value
N_H (10^{22} cm^{-2})	12.2 (11.9–12.6)
Z_{Fe} *	1.35 (1.23–1.47)
Photon index	1.41 (1.38–1.44)
Flux[†] (photons cm^{-2} s^{-1})	1.73×10^{-2}
Luminosity[‡] (erg s^{-1})	2.60×10^{36}
6.4-keV line:	
Flux (counts s^{-1})	$< 5.8 \times 10^{-3}$
$EW_{6.4\,keV}$ (eV)	< 7.8
$\chi^2/d.o.f$	243/170

Notes. The errors are at the 90% confidence level.
* Iron abundance in units of solar. The abundances of the other elements are fixed to the solar values.
[†] Observed flux in the 2.5–12.0 keV band.
[‡] Absorption-corrected luminosity in the 2.5–12.0 keV band at the distance of 8.5 kpc.

to the background fluctuation to the statistical error, we find that the upper-limit of $EW_{6.4\,keV}$ is 8 eV.

3.4. Spectrum of G 359.12−0.05

We extract the spectrum of G 359.12−0.05 from the source region of the solid ellipse in figure 3a, excluding the circular region of 4′-radius around the GA and the elliptical region of the other source M 359.23−0.04 (figure 3b). The background spectrum is made from the two regions with no local enhancement in the 2.45-keV, 6.4-keV and 6.7-keV line images (the dashed areas). The background-subtracted spectra are shown in figure 5. We find that the spectrum clearly extends to the hard band and that it shows several emission lines from highly ionized atoms in the soft band.

The line structures in the soft band are due to a hot thin plasma, while the main origin of the hard band X-rays is spill-over of the GA flux due to the tail of the PSF of the XRT. Using the best-fit spectra of the GA (table 2),

we simulate the spill-over flux and spectrum by the ray-tracing software (`xissimarfgen`). We then fit the spectra with the model of an absorbed thin thermal plasma (VAPEC in XSPEC) plus the spill-over component. The best-fit spectrum and parameters are shown in figure 5 and table 3, respectively.

Statistically, the fit is rejected with $\chi^2/d.o.f = 1.54$ ($d.o.f = 166$). In fact, we see a hint of residual excess in the hard band. Two possibilities may be considered for this excess. The first is the under-subtraction of the GCDX plasma of $kT \sim 6.5$ keV, due to possible non-uniformity near the GA. This possibility may be negligible, because we neither see a local enhancement in the 6.7 keV line image (figure 3c) nor a hint of the 6.7-keV line in the G 359.12−0.05 spectrum. Nevertheless, we add a 6.5-keV plasma to the fitting-model, and find that the possible contamination of the GCDX is less than 15% in the 1–10 keV band.

The second possibility is a calibration error of the spill-over component. We therefore allow the spill-over flux to be a free parameter. The fit is improved to $\chi^2/d.o.f = 1.09$ ($d.o.f = 164$). The additional excesses in the hard band are respectively 31% (FI) and 23% (BI) of those estimated with the nominal PSF calibration.

The nominal PSF calibration uncertainties[4] beyond 2′ are 5% and 15% in FI and BI, respectively. We note that the PSF calibration was performed in the on-axis angle and concentric circle regions. Our observations were, on the other hand, performed in the off-axis angle ($\sim 6′$) and the source region is non-concentric around the GA. We hence compare the simulated flux *vs* observed flux using the Seyfert galaxy MCG −5−23−16, which is the 3′.5 off-axis angle observation (Reeves et al. 2007). Unlike the GA in the GCDX, MCG −5−23−16 is located off the Galactic-plane, where the major X-ray background is the cosmic–X-ray background (CXB). The CXB is spatially more uniform than the GCDX. Therefore we can obtain more reliable fluxes on and around the source. We also adopt the non-concentric region from the MCG −5−23−16, the similar region of G 359.12−0.05. Then we compare the flux of the observed data (after the subtraction of the NXB and CXB) and that of the ray-tracing simulation by the `xissim` software. As a result, we find that the disagreements are 21% and 11% in FI and BI, respectively. Extrapolating linearly these values to the off-angle position (6′), we can expect the uncertainties are 36% (FI) and 19% (BI), which are consistent with our best-fit results. Thus the second possibility is very likely.

We should note that any possible hard X-ray excess does not significantly change the best-fit thin thermal plasma model of the soft X-rays within errors at the 90 % confidence level apart from giving a lower plasma temperature by ~ 0.2 keV. This however gives no essential change for the following discussions.

---

[4] http://www.astro.isas.ac.jp/suzaku/doc/suzakumemo/suzakumemo-2008-04.pdf
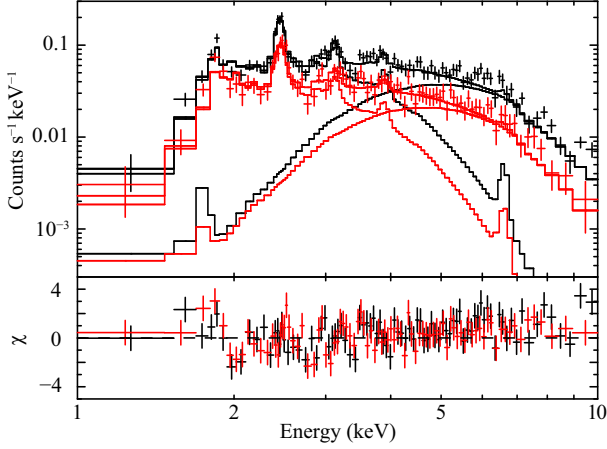
Fig. 5. The background subtracted spectra of G 359.12−0.05 for the FI CCD (black) and BI CCD (red). The solid lines show the models of the absorbed plasma emission and the spill-over component of the GA.

Table 3. Best-fit parameters of G 359.12−0.05

Parameter	Value
$N_{\rm H}$ (10^{22} cm^{-2})	6.7 (6.2–7.3)
kT (keV)	0.93 (0.88–0.98)
$Z_{\rm Si}$ *	1.2 (0.85–1.7)
$Z_{\rm S}$ *	1.4 (1.2–1.7)
$Z_{\rm Ar}$ *	1.5 (1.1–2.1)
Normalization†	6.4 (5.3–7.8)
Flux‡ (photons cm^{-2} s^{-1})	6.3×10^{-4}
$\chi^2/d.o.f$	256/166

Notes. The errors are at the 90% confidence level.
* Abundances in units of solar. The abundance of the other elements are fixed to the solar values.
† Normalization = $(10^{-12}/4\pi D^2) \int n_{\rm e} n_{\rm H} dV$ cm^{-5}, where D, $n_{\rm e}$, and $n_{\rm H}$ are the distance to the G 359.12−0.05, the electron density, and the hydrogen density, respectively.
‡ The observed flux of the plasma emission in the 1.0–10 keV band.

3.5. Spectrum of M 359.23−0.04

We extract the spectrum of M 359.23−0.04 from the region designated in figure 3b. The background region is the same as that for G 359.12−0.05. As shown in figure 6, the spectrum of M 359.23−0.04 is similar to that of G 359.12−0.05. This is reasonable, because M 359.23−0.04 is located in the diffuse emission of G 359.12−0.05. In addition, we find a strong line at 6.4 keV (Fe I Kα) and a hint of Fe I Kβ at 7.1 keV.

We therefore fit the spectrum with the same model of G 359.12−0.05 adding an absorbed power-law plus two Gaussian lines at 6.4 keV and 7.1 keV. The parameters of the plasma model are fixed at those of table 3 except the normalization. The spill-over component of the GA is estimated with the same method as in the analysis of G 359.12−0.05. The best-fit results and parameters are shown in figure 6 and table 4, respectively. For visibility, only the FI spectrum is shown although the FI and BI
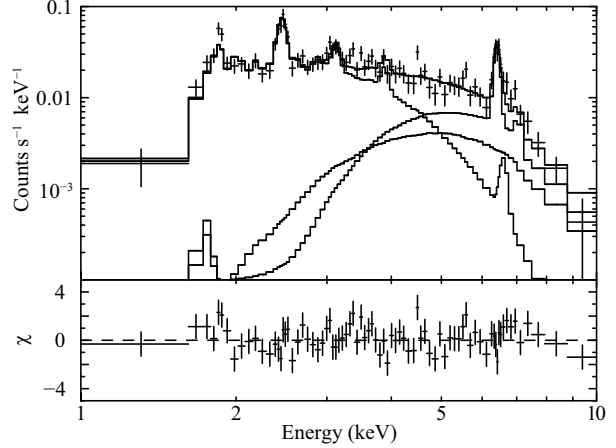

Fig. 6. The XIS background-subtracted FI spectrum of M 359.23−0.04. The solid lines are the best-fit models (see text).

Table 4. Best-fit parameters of M 359.23−0.04

Parameter	Value
$N_{\rm H}$ (10^{22} cm^{-2})	31 (19–35)
Photon index	2.9 (2.2–3.5)
Fe I Kα:	
Center (keV)	6.41 (6.40–6.43)
Line flux*	3.4 (2.6–4.0)
Equivalent width (keV)	1.2 (0.83–1.4)
Fe I Kβ:	
Center (keV)	7.06†
Line flux*	<0.79
Equivalent width (keV)	<0.36
$\chi^2/d.o.f$	164/153

Notes. The errors are at the 90% confidence level.
* In units of 10^{-5} photons cm^{-2} s^{-1}.
† Fixed to $1.1 \times E$ (Fe I Kα).

spectra are fit simultaneously.

As the same reason of G 359.12−0.05, the hard-band flux of M 359.23−0.04 may have some ambiguity due to the uncertainty of the PSF. If we add the same amount of uncertainty (FI:31% and BI:23%) to the spill-over flux of the GA, the power-law continuum associated to the 6.4-keV line decreases by $\sim$ 18%. This modifies the $EW_{6.4\,{\rm keV}}$ value from 1.2 (0.83–1.4) keV to 1.4 (1.1–1.7) keV.

4. Discussion

4.1. Nature of M 359.23−0.04

From the radio MC observation of CS(J=1–0) (Tsuboi et al. 1999), we find that at least one clump of the MCs is associated with M 359.23−0.04 in the two velocity bands: the −140 to −120 km s^{-1} band and −20 to 0 km s^{-1} band. Figure 7 shows the radio contours overlaid on the X-ray images. We find several clumps of MCs and designate them as MC1–6. Among them, MC2 and MC3 are possibly associated with M 359.23−0.04.
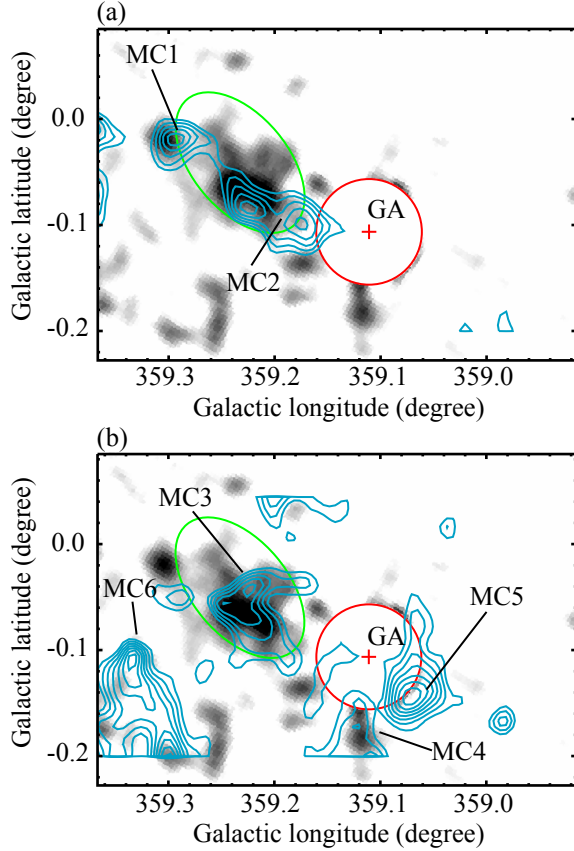
Fig. 7. The 6.4-keV line images (same as figure 3b) are shown in the gray scale. The blue contours trace the CS(J=1-0) radio observation (Tsuboi et al. 1999) in the velocity bands of -140 to -120 km s^{-1} (a), and in the -20 to -0 km s^{-1} (b). The green ellipse shows the source region of M 359.23$-$0.04. The red circle and cross indicate the 3$'$-radius region and the position of the GA, respectively. Individual prominent spots (clumps) in the radio contours are labeled as MC1 to MC6 (see text).

The best-fit $EW_{6.4\,\mathrm{keV}}$ of M 359.23$-$0.04 is 1.2–1.4 keV (see table 4 and section 3.5). This value is naturally explained by the X-ray irradiation (the X-ray reflection nebula: XRN model) on the MC with one solar abundance (e.g., Murakami et al. 2000; Nakajima et al. 2009). If we adopt the electron bombarding model (Yusef-Zadeh et al. 2007; Fukuoka et al. 2009), we need more than 3 solar abundances. The infrared observations (e.g., Davies et al. 2009) argued that the iron abundance of the GC is nearly equal to the solar value. In fact, most of the Suzaku observations of the GC region reported the abundances between 1–2 solar (e.g., Mori et al. 2008, Nobukawa et al. 2008; Tsuru et al. 2009; Nobukawa et al. 2010). Our observation also implies 1.2–1.5 solar abundances in this region (see table 2 and 3). The XRN model is therefore more favorable for the M 359.23$-$0.04 X-ray emission.

In the XRN model, the irradiating source should be very bright or be located near at M 359.23$-$0.04. Thus the GA at a projected distance of 6$'$ from M 359.23$-$0.04 and the past bright Sgr A* (e.g., Inui et al. 2009) are the possible

candidates for the irradiating source. Another possible candidate is a transient source. Although this possibility due to an unknown transient is not excluded, the available observations place this possibility to be a less plausible hypothesis, because no bright transient source has been so far reported from the close vicinity of M 359.23$-$0.04 (e.g.,in't Zand 2001; Sakano et al. 2002; Muno et al. 2009).

Based on the observed profile (figure 3b), the projected shape of M 359.23$-$0.04 is approximated with an ellipse of 12.5 pc $\times$ 22.5 pc (minor $\times$ major axis). Adopting a reasonable assumption that the 3-dimensional structure of M 359.23$-$0.04 is a prolate spheroid with the line-of-sight depth of 12.5 pc (the same as the minor axis), we estimate the volume to be 5×10^{58} cm^3 (a prolate spheroid with axises of 12.5 pc $\times$ 12.5 pc $\times$ 22.5 pc). The observed N_H is (19–35) $\times 10^{22}$ cm^{-2}. On the other hand, the past studies reported that the interstellar absorption to the GC region is $N_\mathrm{H} = 6 \times 10^{22}$ cm^{-2} (Sakano et al. 2002; Ryu et al. 2009). To confirm this value, we conduct the model fitting of the GCDX in the close vicinity of the GA. We then find that the interstellar absorption is $N_\mathrm{H} = 5.7$ (5.5–6.0) $\times 10^{22}$ cm^{-2}, which is consistent with the values in the references. Subtracting the interstellar absorption to the GC region, we estimate that the intrinsic N_H is about $(1-3) \times 10^{23}$ cm^{-2}. On the other hand, N_H of MC2 or MC3, a counterpart of M 359.23$-$0.04 is $\sim 1 \times 10^{23}$ cm^{-2} from the CS(J=1–0) observation (Tsuboi et al. 1999). Thus N_H of the cloud is in the range of $(1-3) \times 10^{23}$ cm^{-2}.

Adopting these physical parameters and assuming that the distances of M 359.23$-$0.04 from the GA and Sgr A* are the same as the projected distances, we estimate the required luminosity of the GA and Sgr A* to produce the 6.4-keV-line flux of M 359.23$-$0.04. In this process, the spectrum shapes of the GA and Sgr A* are assumed to be a power-law with photon index $\Gamma = 1.4$ and 2, respectively (see table 2 and Murakami et al. 2000). The 6.4-keV-fluorescence line is due to X-rays above the iron K-edge energy at 7.1 keV (Murakami et al. 2000). At these high energy X-rays, we can ignore the interstellar absorption between the irradiating source and the XRN. The results of the required luminosity in the 2.5–12 keV band for the GA and Sgr A* are 4×10^{36} erg s^{-1} and 5×10^{38} erg s^{-1}, respectively.

The observed luminosity of the GA is smaller by a factor of 2 than the required luminosity (see table 2). This difference is within the systematic errors of the size, density and distance; i.e., the real distance would be larger than the projected distance. In addition, the flux-variation of the GA by a factor of 2–5 was reported in the long time period (Churazov et al. 1993b; Sakano et al. 1999; Smith et al. 2002). Thus the scenario of the GA origin is consistent with the observed results.

The other possibility, the past flare of Sgr A*, has been proposed for many other 6.4-keV clumps in the GC region (e.g., Nobukawa et al. 2008; Nakajima et al. 2009). The same argument can also be applied to M 359.23$-$0.04, and thus the scenario of Sgr A* origin is possible.

In figure 7, we find other 6.4-keV clumps at near MC1

and MC4. The 6.4-keV fluxes of them are ~ 2 times fainter than that of M 359.23$-$0.04, and hence the physical association is less clear. The other MCs, MC5 and MC6, show no association to the 6.4-keV emissions. These features may not be surprising, if the putative past flare was variable in the time scale of a few years (Koyama et al. 2009).

On the other hand, the scenario of the GA origin can be more easily assessed, if the real distances (not projected distances) of these clumps from the GA are 1.4 times larger than those of MC2 or MC3, because the 6.4-keV fluxes from MC1, MC4, MC5, and MC6 are less than half of those from MC2 or MC3.

4.2.   Nature of the GA

The observed column density of the GA is $N_{\rm H} = 12 \times 10^{22}$ cm^{-2}. If the GA is associated with M 359.23$-$0.04 (see section 4.1), the GA lies in the GC region, because Tsuboi et al. (1999) showed that MCs of CS(J=1–0) are in the GC region. In this case, the large $N_{\rm H}$ of the GA is explained by intrinsic absorption (Kawai et al. 1988) of the order of 10^{23} cm^{-2}.

We constrain the upper-limit for the $EW_{6.4\,\rm keV}$ of 8 eV. The iron abundance is also accurately determined to be 1.38–1.44 solar. If the GA is fully covered by the gas for $\Omega = 4\pi$ steradian, the upper-limit of $EW_{6.4\,\rm keV} = 8$ eV constrains the column density of the circumstellar gas within 7.5 pc (3$'$ at 8.5 kpc) to be $N_{\rm H} \leq 4 \times 10^{21}$ cm^{-2} (Inoue 1985). The implication of the small value of $EW_{6.4\,\rm keV}$ was discussed in detail by Sakano et al. (1999). Here we discuss briefly following Sakano et al. (1999), based on the more severe constraint of $EW_{6.4\,\rm keV}$ ($EW_{6.4\,\rm keV} = 15$ eV in Sakano et al. 1999 vs 8 eV in our case). The $EW_{6.4\,\rm keV}$ of 8 eV implies that the local density near the GA is less than 2×10^2 H cm^{-3}. From figure 6 of Sakano et al. (1999), the velocity of the GA must be less than 7 km s^{-1} under the Bondi-Hoyle accretion mechanism even if the GA has the mass of 20 $M_\odot$. Since no data of the velocity dispersion for a black hole are available, we refer to that of the radio pulsars (neutron stars) from Faucher-Giguère & Kaspi (2006). We then conclude that the possibility of the GA with a smaller velocity than 7 km s^{-1} is only 2×10^{-3}%. Thus the Bondi-Hoyle accretion for the GA is extremely unlikely.

Although the observed $EW_{6.4\,\rm keV} < 8$ eV gives the column density of the circumstellar gas within 7.5 pc to be $N_{\rm H} \leq 4 \times 10^{21}$ cm^{-2} (this value is averaged over 4π steradian), the intrinsic $N_{\rm H}$ determined from the low energy absorption is in the order of 10^{23} cm^{-2}. Thus the large circumstellar gas should be localized in front of the GA. Bally & Leventhal (1991) reported that an MC is associated to the GA, but no MC is found in the line of sight to the GA from Tsuboi et al. (1999). This inconsistency may come from the poor spatial resolution of the former observation. In fact, the spatial resolution of the former observation is $\sim 2'$, while the latter is $\sim 0\overset{\prime}{.}5$. Our implication is consistent with Tsuboi et al. (1999), and hence one possible scenario for the large absorption is due to an accreting gas; the GA is a binary system with a nearly
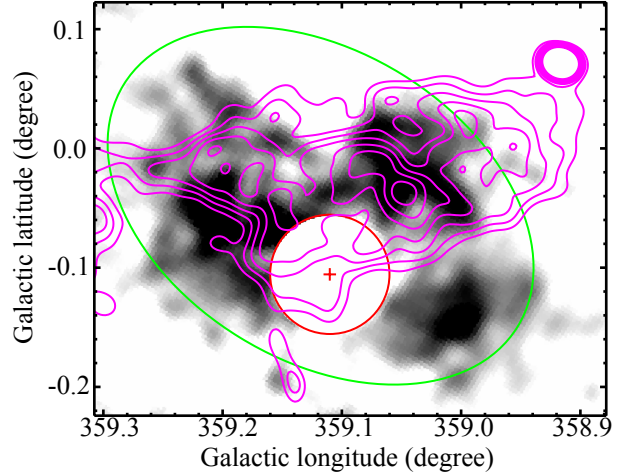

Fig. 8. The 2.45-keV line image (same as figure 3a) is shown in the gray scale. The magenta contours trace G 359.07$-$0.02 from the 90 cm radio continuum observation (LaRosa et al. 2000). The green ellipse shows the source region of G 359.12$-$0.05. The red circle and cross indicate the 3$'$-radius region and the position of the GA, respectively.

edge-on accretion disk.

4.3.   Plasma Parameters of G 359.12$-$0.05

The observed column density of G 359.12$-$0.05 $N_{\rm H} = 6.7 \times 10^{22}$ cm^{-2} is the same as the GC typical column density of $N_{\rm H} = 6 \times 10^{22}$ cm^{-2}, and hence G 359.12$-$0.05 is likely to be in the GC region. Since the source area is ~ 140 arcmin$^2 = 8.1 \times 10^{39}$ cm^2 (at 8.5 kpc), the volume of the plasma is estimated as $\sim (8.1 \times 10^{39}$ cm$^2)^{\frac{3}{2}} = 7.3 \times 10^{59}$ cm^3. Using the filling factor of f, we estimate the electron density, total mass, and total thermal energy to be $n_{\rm e} \sim 0.3\ f^{-\frac{1}{2}}$ cm^{-3}, $M \sim 2 \times 10^2\ f^{\frac{1}{2}}\ M_\odot$, and $E_{\rm th} \sim 1 \times 10^{51}\ f^{\frac{1}{2}}$ erg, respectively.

The estimated mass and thermal energy are slightly larger than those of the other SNRs in the GC region, but are consistent with those of a single SNR. As shown in figure 8, the radio SNR candidate G 359.07$-$0.02 (LaRosa et al. 2000) coincides in position with G 359.12$-$0.05. We therefore propose that G 359.12$-$0.05 is an X-ray counterpart of G 359.07$-$0.02. The thin thermal plasma spectrum and the physical parameters place G 359.12$-$0.05 to be an X-ray SNR in the GC region. From the size of $\sim 9.0 \times 10^{19}$ cm and the sound velocity of $\sim 5 \times 10^7$ cm s^{-1} ($kT \sim 0.9$ keV), the age of this SNR is estimated to be $\sim 6 \times 10^4$ years.

If the GA is also located in the GC region (see section 4.2), G 359.12$-$0.05 may be physically associated with the GA. Then the GA would be a rare system which shows the association of a black hole and an SNR. A similar system is SS433 and the radio SNR W50 (e.g., Safi-Harb & Oegelman 1997). The nature of SS433 is debatable but is a potential candidate of a black hole. On the other hand, the GA is a more established black-hole candidate. Thus our result provides a unique case of the association between a black hole and an X-ray SNR.

5. Summary

1. The equivalent width of the 6.4-keV line of the GA is most severely constrained.
2. We discover two diffuse emissions, $G\,359.12-0.05$ and $M\,359.23-0.04$, around the GA.
3. $G\,359.12-0.05$ is an X-ray counterpart of $G\,359.07-0.02$, and a middle-aged SNR in the GC region.
4. $M\,359.23-0.04$ is likely an XRN illuminated by either the GA or $\mathrm{Sgr\,A^*}$. In the former case, the GA is located in the GC region. This may suggest the association of a Galactic black hole with an SNR.

References

Anders, E., & Grevesse, N. 1989, Geochim. Cosmochim. Acta, 53, 197

Bally, J., & Leventhal, M. 1991, Nature, 353, 234

Bałucinska-Church, M., & McCammon, D. 1992, ApJ, 400, 699

Bondi, H., & Hoyle, F. 1944, MNRAS, 104, 273

Bouchet, L., et al. 1991, ApJL, 383, L45

Bouchet, L., del Santo, M., Jourdain, E., Roques, J. P., Bazzano, A., & DeCesare, G. 2009, ApJ, 693, 1871

Cheng, L. X., Leventhal, M., Smith, D. M., Gehrels, N., Tueller, J., & Fishman, G. 1998, ApJ, 503, 809

Churazov, E., et al. 1993a, A&AS, 97, 173

Churazov, E., et al. 1993b, ApJ, 407, 752

Churazov, E., Gilfanov, M., & Sunyaev, R. 1996, ApJL, 464, L71

Cook, W. R., Grunsfeld, J. M., Heindl, W. A., Palmer, D. M., Prince, T. A., Schindler, S. M., & Stone, E. C. 1991, ApJL, 372, L75

Cordier, B., et al. 1993, A&A, 275, L1

Cui, W., et al. 2001, ApJ, 548, 394

Davies, B., Origlia, L., Kudritzki, R.-P., Figer, D. F., Rich, R. M., & Najarro, F. 2009, ApJ, 694, 46

Eikenberry, S. S., Fischer, W. J., Egami, E., & Djorgovski, S. G. 2001, ApJ, 556, 1

Faucher-Giguère, C.-A., & Kaspi, V. M. 2006, ApJ, 643, 332

Fukuoka, R., Koyama, K., Ryu, S. G., & Tsuru, T. G. 2009, PASJ, 61, 593

Gallo, E., & Fender, R. P. 2002, MNRAS, 337, 869

Harris, M. J., Share, G. H., & Leising, M. D. 1994, ApJ, 433, 87

Hertz, P., & Grindlay, J. E. 1984, ApJ, 278, 137

Hyodo, Y., Tsujimoto, M., Hamaguchi, K., Koyama, K., Kitamoto, S., Maeda, Y., Tsuboi, Y., & Ezoe, Y. 2008, PASJ, 60, S85

Inoue, H. 1985, Space Science Reviews, 40, 317

in't Zand, J. 2001, Exploring the Gamma-Ray Universe, 459, 463

Inui, T., Koyama, K., Matsumoto, H., & Tsuru, T. G. 2009, PASJ, 61, S241

Jung, G. V., et al. 1995, A&A, 295, L23

Kawai, N., Fenimore, E. E., Middleditch, J., Cruddace, R. G., Fritz, G. G., Snyder, W. A., & Ulmer, M. P. 1988, ApJ, 330, 130

Koyama, K., Awaki, H., Kunieda, H., Takano, S., & Tawara, Y. 1989, Nature, 339, 603

Koyama, K., Maeda, Y., Sonobe, T., Takeshima, T., Tanaka, Y., & Yamauchi, S. 1996, PASJ, 48, 249

Koyama, K., et al. 2007a, PASJ, 59, S23

Koyama, K., et al. 2007b, PASJ, 59, S245

Koyama, K., Takikawa, Y., Hyodo, Y., Inui, T., Nobukawa, M., Matsumoto, H., & Tsuru, T. G. 2009, PASJ, 61, S255

Kubota, A., et al. 2007, PASJ, 59, S185

LaRosa, T. N., Kassim, N. E., Lazio, T. J. W., & Hyman, S. D. 2000, AJ, 119, 207

Mirabel, I. F., Paul, J., Cordier, B., Morris, M., & Wink, J. 1991, A&A, 251, L43

Mirabel, I. F., Rodriguez, L. F., Cordier, B., Paul, J., & Lebrun, F. 1992, Nature, 358, 215

Mitsuda, K., et al. 2007, PASJ, 59, S1

Mori, H., Tsuru, T. G., Hyodo, Y., Koyama, K., & Senda, A. 2008, PASJ, 60, S183

Muno, M. P., Bauer, F. E., Bandyopadhyay, R. M., & Wang, Q. D. 2006, ApJS, 165, 173

Muno, M. P., et al. 2009, ApJS, 181, 110

Murakami, H., Koyama, K., Sakano, M., Tsujimoto, M., & Maeda, Y. 2000, ApJ, 534, 283

Nakajima, H., Tsuru, T. G., Nobukawa, M., Matsumoto, H., Koyama, K., Murakami, H., Senda, A., & Yamauchi, S. 2009, PASJ, 61, S233

Nobukawa, M., et al. 2008, PASJ, 60, S191

Nobukawa, M., Koyama, K., Tsuru, T. G. Ryu, S. G., & Tatischeff, V. 2010, PASJ, 62, (in press)

Reeves, J. N., et al. 2007, PASJ, 59, S301

Ryu, S. G., Koyama, K., Nobukawa, M., Fukuoka, R., & Tsuru, T. G. 2009, PASJ, 61, 751

Sakano, M., Imanishi, K., Tsujimoto, M., Koyama, K., & Maeda, Y. 1999, ApJ, 520, 316

Sakano, M., Koyama, K., Murakami, H., Maeda, Y., & Yamauchi, S. 2002, ApJS, 138, 19

Safi-Harb, S., & Oegelman, H. 1997, ApJ, 483, 868

Sawada, M., Tsujimoto, M., Koyama, K., Law, C. J., Tsuru, T. G., & Hyodo, Y. 2009, PASJ, 61, S209

Serlemitsos, P. J., et al. 2007, PASJ, 59, S9

Skinner, G. K., Willmore, A. P., Eyles, C. J., Bertram, D., & Church, M. J. 1987, Nature, 330, 544

Skinner, G. K., et al. 1991, A&A, 252, 172

Smith, D. M., Leventhal, M., Cavallo, R., Gehrels, N., Tueller, J., & Fishman, G. 1996, ApJ, 458, 576

Smith, D. M., Heindl, W. A., & Swank, J. H. 2002, ApJL, 578, L129

Sunyaev, R., et al. 1991, ApJL, 383, L49

Tsuboi, M., Handa, T., & Ukita, N. 1999, ApJS, 120, 1

Tsuru, T. G., Nobukawa, M., Nakajima, H., Matsumoto, H., Koyama, K., & Yamauchi, S. 2009, PASJ, 61, S219

Uchiyama, Y., et al. 2008, PASJ, 60, S35

Uchiyama, H., et al. 2009, PASJ, 61, S9

Yamauchi, S., Kawada, M., Koyama, K., Kunieda, H., & Tawara, Y. 1990, ApJ, 365, 532

Yusef-Zadeh, F., Muno, M., Wardle, M., & Lis, D. C. 2007, ApJ, 656, 847